One-pot synthesis of highly dispersed mesoporous Cu/ZrO$_2$ catalysts for NH$_3$-SCR

Ole Håvik Bjørkedal [a], Samuel Konrad Regli [a,b], Rob Jeremiah G. Nuguid [b,c], Per Erik Vullum [d], Oliver Kröcher [b,c], Davide Ferri [b], Magnus Rønning [a,*]

[a] Department of Chemical Engineering, Norwegian University of Science and Technology, NO-7491 Trondheim, Norway
[b] Paul Scherrer Institut, CH-5232 Villigen PSI, Switzerland
[c] Institute of Chemical Sciences and Engineering, École polytechnique fédérale de Lausanne (EPFL), CH-1015 Lausanne, Switzerland
[d] SINTEF Industry, Trondheim, Norway

ARTICLE INFO

ABSTRACT

Catalysts consisting of highly dispersed copper on a mesoporous ZrO$_2$ support were synthesised via a one-pot sol-gel synthesis and were tested for the selective catalytic reduction of NO$_x$ by NH$_3$. The copper dispersion was investigated by XRD and TEM, which showed no discernible copper oxide particles up to 6 wt% Cu, while they were detected at 15 wt% Cu.

NH$_3$ adsorption and the SCR reaction were followed *in situ* by diffuse reflectance infrared Fourier transform spectroscopy (DRIFTS) on mesoporous ZrO$_2$ and on one-pot synthesized 3 wt% Cu/ZrO$_2$. Cu was found to improve the NH$_3$ adsorption capacity of the catalyst by enhancing the Lewis functionality.

The catalysts were efficient for SCR at low temperature, at 150 °C 75% of NO was converted over 6 wt% Cu/ZrO$_2$ at water-free conditions. Increasing the copper loading while maintaining the dispersion improved NO$_x$ conversion.

1. Introduction

Nitrogen oxides (NO and NO$_2$, abbreviated: NO$_x$) are gases that can have a harmful effect on both health and environment when released in the atmosphere. Combustion processes in transportation and industry are substantial sources of NO$_x$, where they are produced in a gas phase reaction between N$_2$ and O$_2$ at high temperature. Therefore, NO$_x$-generation is not directly dependent on the combustion fuel, but is determined by operating conditions such as the air-to-fuel ratio and temperature of the combustion process [1]. Emissions of NO$_x$ have a particular effect on the overall air quality of densely populated areas and urban centers, as there are many small sources, such as cars, trucks and ships, that contribute to a substantial amount of the overall emissions. Therefore, it is important to efficiently limit the NO$_x$-emissions close to the source for both stationary and mobile emitters.

Selective Catalytic Reduction (SCR) is an important method for reducing NO$_x$ emissions in stationary and mobile applications. In the last decades there has been a major research effort to develop more efficient SCR catalysts, especially for the transportation sector due to the more stringent regulations on diesel engine emissions. The SCR process is based on three main reactions, commonly referred to as standard SCR (1), fast SCR (2) and NO$_2$-SCR (3) [2].

$$4NO + 4NH_3 + O_2 \rightarrow 4N_2 + 6H_2O \qquad (1)$$

$$NO + NO_2 + 2NH_3 \rightarrow 2N_2 + 3H_2O \qquad (2)$$

$$6NO_2 + 8NH_3 \rightarrow 7N_2 + 12H_2O \qquad (3)$$

The demand for efficient de-NO$_x$ systems has lead to the development of several classes of SCR catalysts. Notable examples are copper-exchanged chabazites (Cu-CHA) such as Cu-SSZ-13. These catalysts have been successfully commercialized due to their efficiency at low temperature and hydrothermal stability [3–8]. The nature of the active site in these catalysts has been extensively researched, but it is generally claimed that it is a single Cu site in the cage of the zeolite structure [8–11]. Although Cu-CHA is established as a well-functioning catalyst for automotive SCR, other catalytic designs are still being researched [12]. Automotive SCR has to be efficient for a wide range of operating conditions, as the operating conditions are dictated by the dynamic

operation of the engine. Common objectives for SCR catalyst development include obtaining high efficiency across a wide temperature range, especially at low temperatures. Other important factors are the stability, selectivity and lifetime of the catalyst. Copper supported on various metal oxides are among the materials that have been proposed as catalysts for SCR, but the formation of copper oxide particles have been found to be a disadvantage for SCR [12–15].

The copper oxide particle size on a metal oxide support is typically closely connected to the loading of copper on the catalyst, and it is generally hard to maintain small particle sizes while increasing the loading. However, there are examples of sol-gel syntheses of catalysts that produce well-dispersed supported metal oxides at relatively high metal loading. The synthesis of mesoporous silica [16] by surfactant-directed sol-gel synthesis opened up new opportunities for synthesis of porous materials with specific pore properties. The surfactants are used as structure directing agents by allowing the surfactants to form cylindrical micelles with a specific diameter through Evaporation-Induced Self Assembly (EISA) [17]. It has been demonstrated that the sol-gel synthesis method can be exploited to introduce an active metal into the pores of the structure. A hydrophobic metal precursor mixed with the surfactants places the metal precursor among the micelles, and therefore at the core of the pores as these are formed, allowing for a one-step synthesis of the catalyst [18,19]. An advantage of this one-step synthesis principle is that it bypasses the transport limitations in e.g. impregnation, ion exchange and other traditional catalyst synthesis methods, as well as facilitate very high metal dispersion at high loading [20].

Zirconia (ZrO_2) is a hydrothermally stable metal oxide that has successfully been used as a support material in redox catalysis. Notable examples are ceria-zirconia supports in the three-way converter, as part of mixed oxide SCR catalysts [21], and has also been tested as a support material for NO_2 adsorption [22–24] and SCR catalysis [15,25–29]. Due to these properties, ZrO_2 was chosen as the support material for this study.

Pietrogiacomi et.al. [30] prepared CuO_x/ZrO_2 by adsorption or impregnation methods, and found that the reaction rate of NO was proportional to Cu content up to a Cu loading of 1.53 wt%, at the point of which CuO-particles were observed. This effect was observed independently of the preparation method used. These results suggest that increased loading could improve SCR efficiency as long as high Cu dispersion is maintained. Djerad et.al. [31] produced ZrO_2-supported catalysts based on conventional ZrO_2 and a mesoporous ZrO_2 support synthesized by a sol-gel method. Both of these supports were impregnated with Fe_2O_3. Here, the mesoporous ZrO_2 support was found to enhance the SCR activity of the catalyst. A recent publication by Świrk et.al. [32] presented a one-pot synthesis of ZrO_2-supported Cu and Fe SCR catalysts with up to 3% metal loading where the metal was well dispersed on the support. These Cu/ZrO_2 catalysts showed promising low temperature activity for SCR.

Here, we investigate the possibility of increasing the copper loading on the support while maintaining a high dispersion of copper, thereby increasing the density of surface active sites.

Because of the complexity of the interaction between the mesoporous ZrO_2, the copper and the reactants under SCR conditions, it is difficult to distinguish the role of each component in the reaction mechanism and to identify the intermediate species. Hence, it is important to separately investigate the interaction of each reactant with the catalyst. Here, we report the investigation of the NH_3 and NO interaction with the ZrO_2 and 3 wt% Cu/ZrO_2 catalyst, by diffuse reflectance infrared Fourier transform spectroscopy (DRIFTS), which is sensitive to the interaction of NH_3 and NO with different adsorption sites.

2. Methods

The catalysts were synthesized by an EISA sol-gel method, developed and adapted from similar syntheses for mesoporous metal oxides [33–36]. 14.039 g Zirconium(IV) propoxide ($Zr(OCH(CH_3)_2)_4$), 70 wt% solution in 1-propanol) was mixed with 30 mL absolute ethanol and 3.0 mL HNO_3 (70%) and stirred thoroughly. In a separate beaker, 3.0 g Pluronic F127 and the appropriate amount of copper(II) acetylacetonate ($Cu(C_5H_7O_2)_2$) was dissolved in 30 mL absolute ethanol and 1.5 mL HNO_3 (70%). The two solutions were mixed and stirred vigorously for 4 h at room temperature. The solution was then set to age at 60 °C for three days until a dry, porous gel was formed. The gel was calcined in air at 600 °C for 4 h, by ramping up the temperature by 1.0 °C min^{-1}. The samples are referred to as "x%Cu/ZrO$_2$", where x is the copper loading in wt%. A ZrO_2 sample without copper was synthesized following the same procedure, except the addition of copper(II) acetylacetonate. This sample is referred to as "ZrO_2".

Surface area and pore characteristics were determined by N_2 physisorption, using the Brunauer, Emmett & Teller (BET) [37] and Barrett, Joyner, Halenda (BJH) models [38]. The samples were degassed under vacuum at 200 °C overnight before being analyzed at 77 K using a Micromeritics Tristar II 3020 Surface Area and Porosity Analyzer.

X-ray diffraction (XRD) was performed with a Bruker D8 Advance X-ray Diffractometer using Cu $K\alpha$ radiation source with wavelength 1.54060 Å. The 2θ-range of the scans were 5° to 75° with a step size of 0.045°. The obtained patterns were compared with references from Crystallography Open Database (COD) [39–45]. The following reference patterns with COD number and citation were used: Cubic ZrO_2 (COD 1521753) [46], monoclinic ZrO_2 (COD 9007448) [47], and monoclinic CuO (COD 1011148) [48].

Transmission electron microscopy (TEM) samples were prepared by crushing the catalysts to a fine powder, dispering them in 96 vol% ethanol, sonicating for 10 min, and transferring a drop of the resulting dispersion onto a holey carbon Cu TEM grid. TEM and Low Angle Annular Dark Field Scanning Transmission Electron Microscopy (LAADF-STEM) was performed with a double Cs aberration corrected coldFEG JEOL ARM 200F operated at 200 kV. Simultaneous Energy Dispersion X-ray Spectroscopy (EDS) and dual Electron Energy Loss Spectroscopy (EELS) were performed in Scanning Transmission Electron Microscopy (STEM) mode. The microscope is equipped with a 100-mm^2 large solid angle (0.98 srad) Centurio detector for EDS and a Quantum ER for EELS.

SCR experiments were performed in a stainless steel fixed bed reactor (0.9 cm inner diameter). For each experiment 0.3 g of the powder sample was diluted with 3.2 g SiC to minimize flow and heat transfer limitations in the catalyst bed. Both the sample and SiC was sieved to a particle size range of 53 to 90 μm. The feed gas composition was 600 ppm NO, 600 ppm NH_3, 10 vol% O_2, 5 vol% H_2O (when required) and balance Ar at ambient pressure. For some experiments the feed concentration of NH_3 was varied, while maintaining the concentration of NO at 600 ppm. The total feed gas flow was kept constant at 250 mL min^{-1} for all experiments (GHSV = 58333 h^{-1}). The outlet gases were measured on-line with a mass spectrometer (Hiden Analytical HPR-20 R&D).

Selected samples were aged in the same reactor to determine their hydrothermal stability. This treatment was performed at 500 °C under a flow of 5 vol% H_2O/Ar for three days.

Conversion of NO and NH_3 (X_A) was calculated according to Eq. (4), while N_2 selectivity (S_{N_2}) was determined using Eq. (5) [49].

$$X_A = \frac{[A]_{in} - [A]_{out}}{[A]_{in}} \times 100\% \tag{4}$$

$$S_{N_2} = \frac{[NO]_{in} - [NO]_{out} - [NO_2]_{out} - 2[N_2O]_{out}}{[NO]_{in} - [NO]_{out}} \times 100\% \tag{5}$$

In situ DRIFTS was performed using a Bruker Vertex 70 FT-IR spectrometer equipped with a Harrick Praying Mantis diffuse reflection accessory. The spectra were collected at a resolution of 4 cm^{-1} in the range of 4000–1000 cm^{-1} by accumulating 50 (background) and 10 (sample) interferograms using a scanner velocity of 80 kHz. The sample

was mounted into a custom-built spectroscopic cell [50] equipped with a CaF$_2$ window. Sample (mass corresponding to a gas hourly space velocity (GHSV) of 60000 h^{-1}) pretreatment consisted of heating to 450 °C in 5 vol% O$_2$/Ar (100 mL min^{-1}; 10 °C min^{-1}) and cooling after 1 h to 150 °C. Then, a gas mixture containing 5 vol% O$_2$ and 1000 ppm NH$_3$ in Ar was passed through the sample for 30 min, while simultaneously collecting spectra. After purging the gaseous and weakly adsorbed NH$_3$ by 5 vol% O$_2$ in Ar flow for 30 min, a gas mixture containing 5 vol% O$_2$ and 1000 ppm NO in Ar was passed through the sample while spectra were continuously collected.

3. Results and discussion

3.1. Surface area and porosity

Key parameters on pore and surface characteristics are shown in Table 1. The BET surface area of the synthesized samples was found to be in the range of 50–80 m^2 g^{-1} after calcination. While the average pore volume is similar for all samples, there are significant variations in the pore diameter that affect the overall surface area. The BJH pore size distribution of the synthesized samples is shown in Fig. 1. Most of the samples have a well-defined and narrow distribution of pore diameters

Table 1
BET surface area, specific pore volume and average pore size for all samples. Pore volume and diameter calculations were determined using the BJH-model on desorption data. The samples marked "aged" were exposed to a hydrothermal aging procedure under 5 vol% H$_2$O/Ar at 500 °C for three days.

Sample	S_{BET} (m^2 g^{-1})	Pore volume (cm^3 g^{-1})	Average pore diameter (nm)
ZrO$_2$	53	0.10	4.6
3%Cu/ZrO$_2$	57	0.11	4.5
6%Cu/ZrO$_2$	78	0.11	4.0
15%Cu/ZrO$_2$	58	0.11	5.0
3%Cu/ZrO$_2$ aged	29	0.10	9.0
6%Cu/ZrO$_2$ aged	26	0.09	10.7
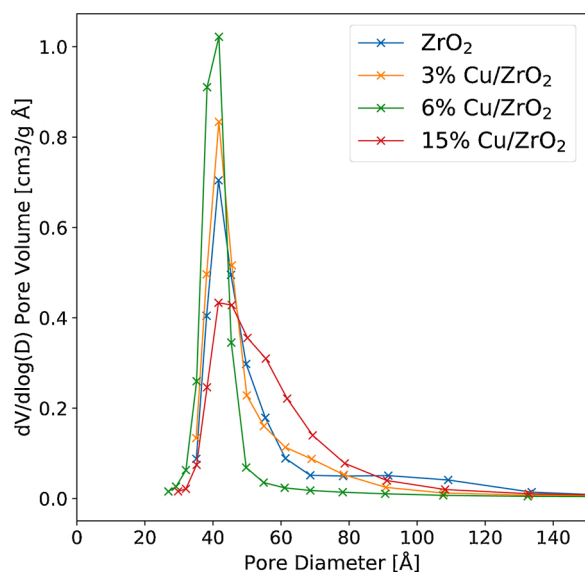
Fig. 1. BJH pore size distributions for the Cu/ZrO$_2$ catalysts and the ZrO$_2$, calculated based on desorption data. The majority of the pores has a diameter of 4-5 nm, corresponding to a typical pore size for F127 as structure directing agent. 15%Cu/ZrO$_2$ has a wider pore size distribution with a larger fraction of the pore volume from pores in the range of 5 nm to 9 nm.

centered at 4–5 nm. This is a typical pore size for systems where F127 is used as the structure directing agent [35]. The main peak is generally not symmetric, as all samples except 6%Cu/ZrO$_2$ show the presence of some pores that are up to 7 to 8 nm in diameter. This effect is most notable for 15%Cu/ZrO$_2$ where the pore size distribution is wider and shifted towards larger pores. It is likely that the pore size for this sample is affected by the formation of larger copper oxide particles.

3.2. Copper dispersion

X-ray diffraction was used to evaluate the overall structure of the samples, as well as to determine if major copper oxide crystallites were formed in the synthesis. The diffractograms are shown in Fig. 2. For 3% Cu/ZrO$_2$ and 6%Cu/ZrO$_2$ there is no visible indication of copper oxide crystallites, and all peaks can be assigned to ZrO$_2$. The copper oxide in these samples is likely well dispersed. In the XRD pattern of 15%Cu/ ZrO$_2$ an additional peak is observed at $2\theta = 39°$, indicating that larger CuO crystallites are present at this copper loading.

TEM images of 6%Cu/ZrO$_2$ and 15%Cu/ZrO$_2$ (Fig. 3) further show the dissimilarity in copper particle size between the two samples. In 15% Cu/ZrO$_2$, copper oxide particles were observed as copper-rich areas in the Cu element maps based on both EELS and EDS. In Fig. 3b the Zr and Cu maps are combined into a color map where Zr and Cu are given in green and red colors, respectively. The same segregation of Cu into Cu-rich particles was not observed for 6%Cu/ZrO$_2$. However, by using LAADF-STEM imaging, which is very sensitive to variations such as additional atoms at the top surface of the sample, it was possible to detect copper atoms by their bright contrast to the ZrO$_2$ background (Fig. 3a).

The electron diffraction patterns of the two samples mirror the observations from XRD. Fig. 3c shows the electron diffraction pattern of 6%Cu/ZrO$_2$. All diffraction rings for 6%Cu/ZrO$_2$ can be indexed according to face centered cubic ZrO$_2$ (space group Fm-3m).

The electron diffraction pattern of 15%Cu/ZrO$_2$ (Fig. 3d) shows additional diffraction rings, which do not match the signal from metallic Cu or ZrO$_2$. All the red rings shown in Fig. 3d are identical to diffraction rings of 6%Cu/ZrO$_2$ (Fig. 3c). The green rings indicate phases of monoclinic ZrO$_2$. From low (small rings) to high 2θ-scattering angles they can be indexed in the following order: (1 0 0), (0 1 1)/(1 1 0), (−1 1 1), (1 11), (0 0 2)/(0 2 0), (−2 1 1), (0 2 2)/(2 2 0). The two blue rings in the pattern are from monoclinic CuO, and can be indexed as (0 0 2)/(−1 1 1) (inner ring) and (1 1 1)/(2 0 0). This outer ring, i.e. Bragg scattering from (1 1 1) or (2 0 0) planes, is unique for CuO and does not overlap with Bragg scattering from cubic or monoclinic ZrO$_2$.

The STEM imaging, together with the X-ray- and electron diffraction analysis, indicates that copper is atomically dispersed at 6% loading, while copper oxide crystallites form at 15% Cu due to the high copper content. It can be assumed that 3%Cu/ZrO$_2$ has a similar dispersion to 6%Cu/ZrO$_2$.

3.3. SCR performance

The catalysts were tested under SCR conditions with and without steam in the feed. The effect of NH$_3$ dosing on the SCR system was also investigated. Lastly, selected samples underwent a hydrothermal treatment to assess the effect of steam and high temperature on the structural properties of the catalysts.

3.3.1. Effect of steam

Fig. 4 shows the results of the steady-state SCR tests on Cu/ZrO$_2$ with varying copper loading with and without steam in the feed. In the absence of steam, the highest conversion of NO was observed at 225 °C, where it is close to 100% for the three samples, but 6%Cu/ZrO$_2$ exhibited the highest NO conversion and selectivity to N$_2$. The conversion of NO gradually decreased above 350 °C, and the selectivity to N$_2$ started to decrease at even lower temperature. However, the NH$_3$
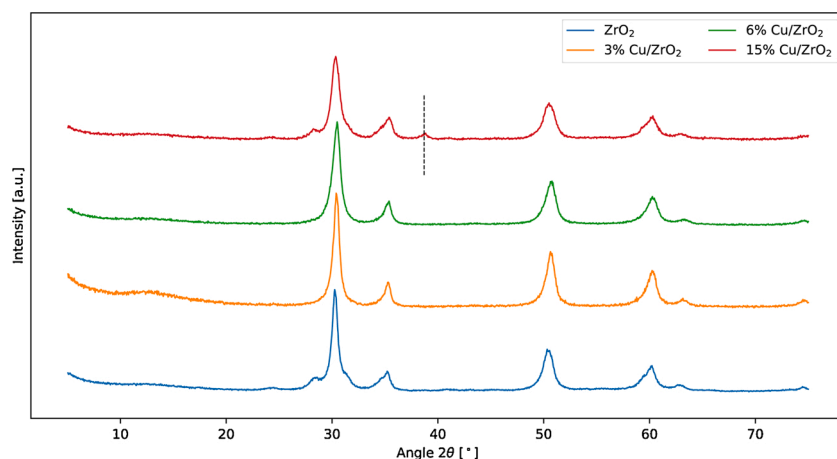
Fig. 2. XRD patterns of all samples as synthesized. The patterns of ZrO_2, 3%Cu/ZrO_2 and 6%Cu/ZrO_2 are very similar, and their peaks can be assigned to ZrO_2 [47, 46]. No peaks related to copper oxide are observed in these samples. 15%Cu/ZrO_2 show an additional peak at $2\theta = 39°$ (marked by dashed line) that can be recognized as a major peak in the CuO reference pattern (COD 1011148) [48].
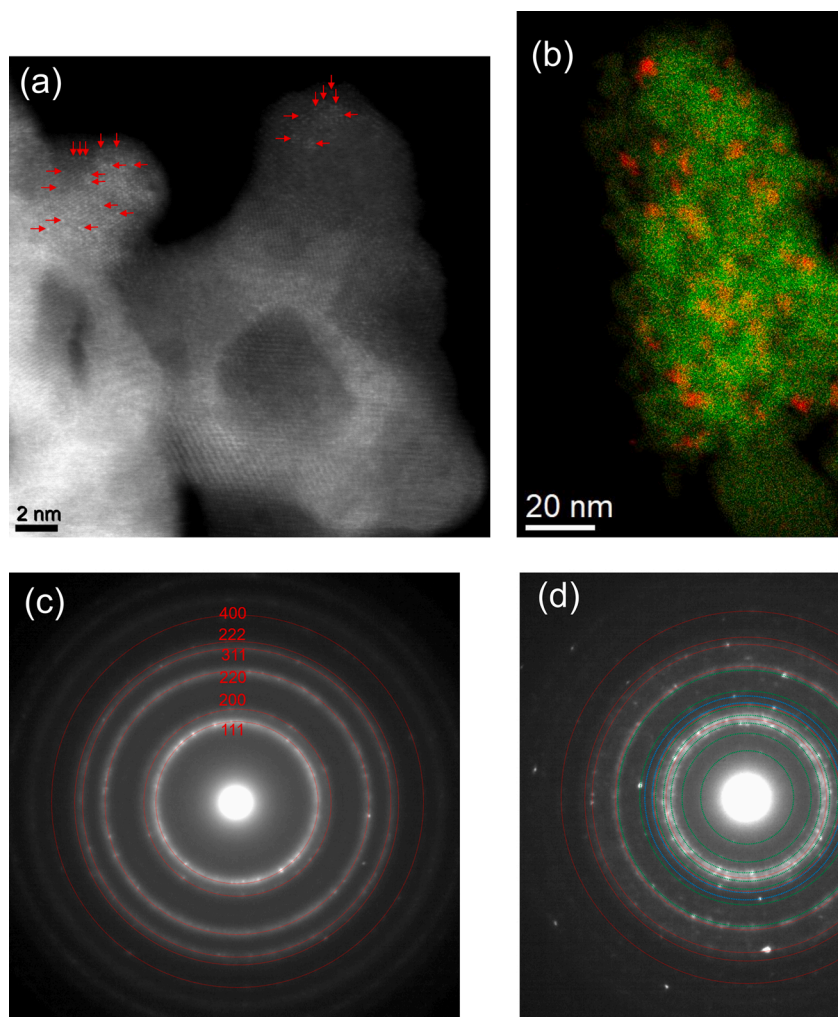

Fig. 3. TEM images of 6%Cu/ZrO_2 and 15% Cu/ZrO_2. **3a:** LAADF STEM image of 6%Cu/ZrO_2 indicating a number of surface atoms in contrast to the ZrO_2 background, most likely Cu atoms. **3b:** EDS-EELS elemental mapping of 15%Cu/ZrO_2 Cu (red) is found in clusters on the zirconia (green) support. Some copper is also detected dispersed among the Zr background. **3c:** Electron diffraction pattern from 6%Cu/ZrO_2. All of the diffraction rings can be indexed as face centered cubic ZrO_2 (marked in red, with hkl indexes). **3d:** Electron diffraction pattern from 15%Cu/ZrO_2. The red rings are identical to the rings shown in Fig. 3c, green rings indicate monoclinic ZrO_2, and blue rings indicate phases that stem from monoclinic CuO. (For interpretation of the references to color in this figure legend, the reader is referred to the web version of this article).

conversion was complete for all samples above 350 °C, suggesting that the decrease in NO conversion is caused by parasitic oxidation of NH_3 [51–55].

H_2O is an unavoidable component of exhaust gas. In general, the conversion of NO and NH_3 is impaired reversibly with steam present in the feed compared to the dry tests. This indicates that H_2O saturates the surface and hinders access to adsorption sites [56,27]. Similar to the tests without steam, the conversion of NO decreased gradually above 350 °C. While full NH_3 conversion was reached at a higher temperature than in the case without steam, parasitic NH_3 oxidation was also present.
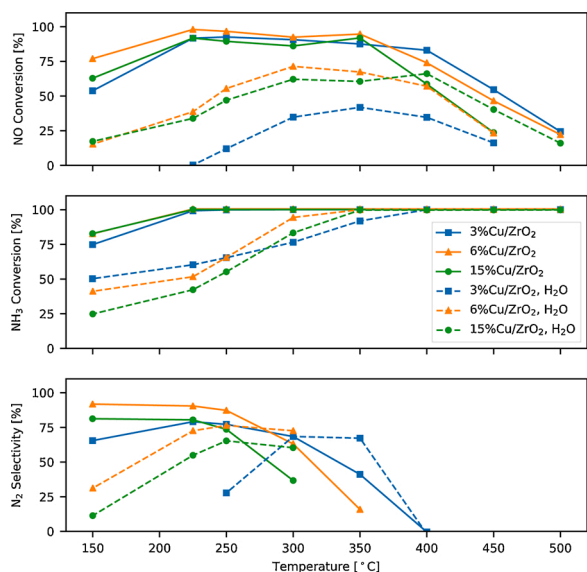
Fig. 4. Steady-state SCR for Cu/ZrO_2 with increasing copper loading with and without steam. NO conversion (top), NH_3 conversion (middle) and N_2 selectivity (bottom) as a function of temperature. Feed conditions: 600 ppm NO, 600 ppm NH_3, 10 vol% O_2, 0 vol% H_2O (solid lines) and 5 vol% H_2O (dashed lines).

In general, 6%Cu/ZrO_2 shows the highest NO conversion rates both with and without steam in the feed. Based on the XRD-patterns shown in Fig. 2, it can be reasonably assumed that copper is dispersed to a similar degree in 3%Cu/ZrO_2 and 6%Cu/ZrO_2. The conversion of NO could therefore be expected to increase with higher copper loading as there should be more available sites on the surface. However, there is not much difference between the samples in terms of NO conversion below 350 °C, except for the significantly lower NO conversion of 3%Cu/ZrO_2 in the presence of steam.

### 3.3.2. Effect of NH_3 feed concentration

The results of the SCR tests shown in Fig. 4 indicate that parasitic NH_3 oxidation inhibits the SCR reaction at high temperature. The detrimental effects of this side reaction are two-fold: Firstly, there is less NH_3 available to act as the reducing agent in the SCR reaction, where the stoichiometric ratio of NO_x to NH_3 is close to 1:1. Secondly, the products of NH_3 oxidation are the unwanted species NO_x and N_2O, besides N_2 [1, 57–59]. Because the dosage of NH_3 is typically controlled in practice, it is interesting to study the effect of the NO:NH_3 ratio in the feed composition on the SCR performance and the influence of side reactions.

Hence, the best-performing catalyst, 3%Cu/ZrO_2, was tested under NH_3 oxidation conditions. Fig. 5 shows the NH_3 conversion and the nitrogen-containing products for an experiment under dry conditions without NO in the feed. Full NH_3 conversion was reached at 300 °C, which is slightly higher than in the SCR experiments. The main product at low temperature was NO. N_2 dominated between 250 °C and 400 °C. In the high temperature range NO and to some extent NO_2 were increasingly produced [51–55]. The concentration of N_2O was comparatively low over the entire temperature range. The low and sometimes negative NO conversion observed in the SCR-experiments at high temperatures was a consequence of the NO_x produced from NH_3 at high temperature.

SCR experiments at doubled NH_3 feed concentration were performed to investigate the effect of over-stoichiometric NH_3. Fig. 6 compares conversion and selectivity under steady state SCR for the three catalysts. Doubling the feed concentration of NH_3 slightly increased NO conversion above 350 °C where full NH_3 conversion was also reached. This could be an effect of a higher partial pressure of NH_3 available for the
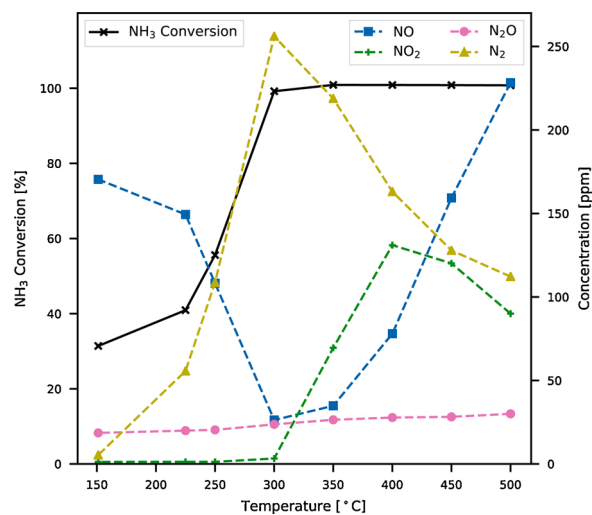

Fig. 5. NH_3 conversion (right axis) and concentration of nitrogen compounds (left axis) for NH_3 oxidation over 3%Cu/ZrO_2. Feed conditions: 600 ppm NH_3, 10 vol% O_2, 0 vol% H_2O.
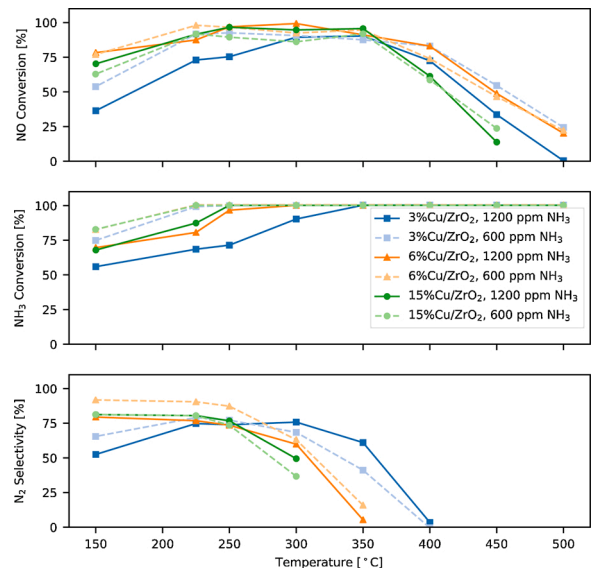
Fig. 6. Steady State SCR with 1:1 (muted colors, dashed lines) and 2:1 (bright colors, solid lines) NH_3:NO feed ratios. NO conversion (top), NH_3 conversion (middle) and N_2 selectivity (bottom) as a function of temperature. Feed conditions: 600 ppm NO, 600 ppm or 1200 ppm NH_3, 10 vol% O_2, 0 vol% H_2O. (For interpretation of the references to color in this figure legend, the reader is referred to the web version of this article.)

SCR-reaction through a larger portion of the catalyst bed. Increasing NH_3 feed concentration impaired the NO conversion at low temperature (T< 300 °C) for 3%Cu/ZrO_2, while the same effect was not seen at higher copper loading.

The effect of NH_3 feed concentration was investigated more closely on 3%Cu/ZrO_2 by comparing the effect of NH_3 shortage and of stoichiometric as well as over-stoichiometric amounts of NH_3. Fig. 7 shows conversion and selectivities for these experiments. The overall NO conversion decreased in the case of NH_3-shortage, which should be expected as the reaction stoichiometry of the SCR reaction is 1:1. Above 350 °C, the decline in NO conversion was less steep for 300 ppm NH_3. In the same temperature range, the N_2 selectivity was highest for the lowest NH_3-feed concentration, while the conversion of NO was less affected. In
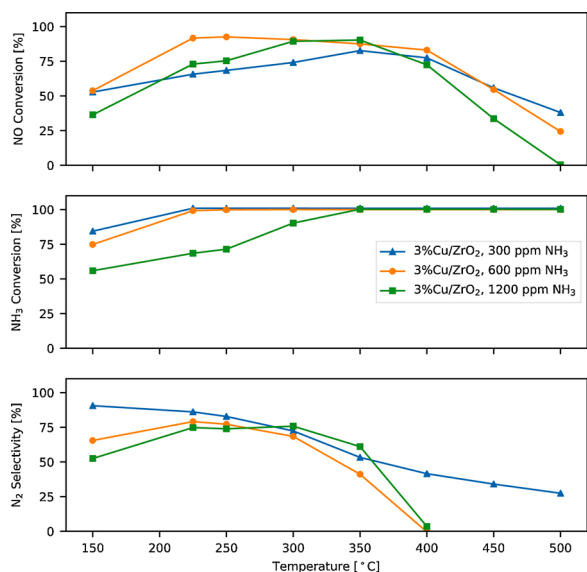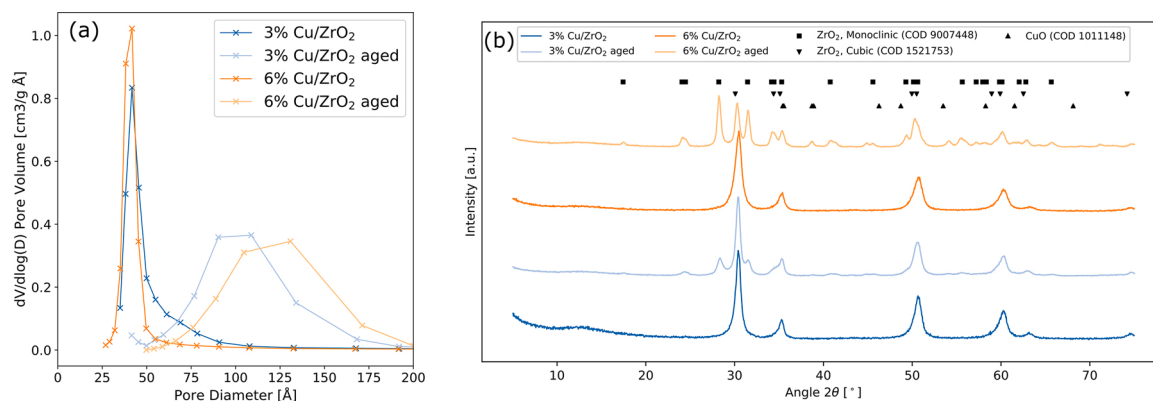
Fig. 7. The effect of half, stoichiometric and double NH_3 feed concentration compared to the NO feed for NO conversion (top), NH_3 conversion (middle) and N_2 selectivity (bottom) as a function of temperature for 3%Cu/ZrO$_2$. Feed conditions: 600 ppm NO, 300, 600 or 1200 ppm NH_3, 10 vol% O_2, 0 vol% H_2O.

this temperature range, NH_3 oxidation can be expected to impact the system, producing species such as N_2O and NO_x. Hence, the attempt to increase the NH_3 partial pressure to compensate the NH_3-loss at higher temperature resulted in even lower N_2 selectivity and NO conversion.

3.3.3. Hydrothermal stability

3%Cu/ZrO$_2$ and 6%Cu/ZrO$_2$ were exposed to a flow of 5 vol% H_2O/Ar at 500 °C for 72 h to assess the effect of heat and steam on the copper dispersion, pore characteristics and SCR efficiency of the catalysts. The pore size distribution of the aged samples (Fig. 8a) shows that the aging procedure has affected the pore structure of the support. The aged samples have a larger average pore size and lower specific surface area (Table 1) than the fresh samples due to sintering.

Fig. 8b compares the diffractograms of the fresh and aged samples. In both aged catalysts the contribution of ZrO$_2$ is more pronounced, and several smaller peaks appear. This is consistent with the increased pore size and reduced surface area obtained from the N_2-physisorption, and

indicates that the hydrothermal treatment increases the ZrO$_2$-crystallite size. Additionally, there were phase transitions from cubic ZrO$_2$ to cubic and monoclinic ZrO$_2$. For 6%Cu/ZrO$_2$ a peak appeared at the same position where copper oxide was observed in 15%Cu/ZrO$_2$ (Fig. 2), indicating that copper sintering has formed some copper oxide crystallites during the hydrothermal treatment that were large enough to be detected by XRD. The same peak was not observed in the case of 3%Cu/ZrO$_2$, which indicates that if copper sintering has occurred, the crystallite size remains relatively small.

The SCR performance of 3%Cu/ZrO$_2$ and 6%Cu/ZrO$_2$ before and after the aging procedure with and without steam is compared in Fig. 9. The NO conversion of the aged samples was slightly lower under all applied conditions, while the conversion of NH_3 was less affected. The N_2 selectivity was generally poor at both low and high temperature under humid conditions, especially for the aged samples. Under dry conditions, the N_2 selectivity was slightly improved at high temperature for the aged samples. While the support structure was substantially affected by the hydrothermal treatment, it does not seem to significantly affect the SCR performance of the catalysts.
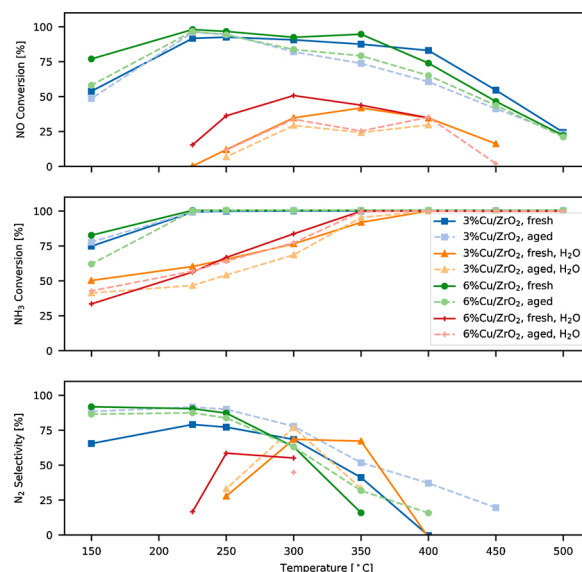
Fig. 9. SCR-performance under dry and humid conditions for 3%Cu/ZrO$_2$ and 6%Cu/ZrO$_2$ before ("fresh") and after ("aged") hydrothermal aging. Feed conditions: 600 ppm NO, 600 ppm NH_3, 10 vol% O_2, 0 vol% or 5 vol% H_2O.

Fig. 8. Pore size distribution and XRD of hydrothermally treated samples. **8a:** Pore size distribution (BJH desorption data) for fresh and aged samples of 3%Cu/ZrO$_2$ and 6%Cu/ZrO$_2$. The pore size increases after the aging procedure. **8b:** XRD comparing 3%Cu/ZrO$_2$ and 6%Cu/ZrO$_2$ before and after aging. Peaks related to monoclinic ZrO$_2$ become more pronounced after hydrothermal aging, indicating a phase transition from cubic to cubic and monoclinic ZrO$_2$. The patterns related to copper oxide are less affected by aging. Reference peaks for monoclinic ZrO$_2$ (COD 9007448) [47], cubic ZrO$_2$ (COD 1521753) [46] and monoclinic CuO (COD 101148) [48] are indicated.

3.4. In situ DRIFTS

3.4.1. NH₃ adsorption

Fig. 10 shows the *in situ* DRIFT spectra obtained during NH₃ adsorption at 150 °C in the presence of oxygen over ZrO₂ and 3%Cu/ZrO₂ over the first 3 min and after 30 min.

Due to the interaction (coordination or hydrogen bonding) with the adsorbed species, the spectra of unloaded ZrO₂ exhibited two major negative hydroxyl bands, namely mono-coordinated (3763 cm⁻¹) and multi-coordinated (3672 cm⁻¹) hydroxyl groups (Fig. 11a) [60,61]. ZrO₂ possesses only Lewis acid functionality as with other unloaded metal oxides such as TiO₂ or Al₂O₃ [62–64], which is reflected by the positive peaks at 3351, 3247, and 1602 cm⁻¹ corresponding to NH₃ coordinated to a metal ion center [65], e.g. Zr⁴⁺. The presence of signals of nitrite (1185 cm⁻¹) and nitrate (1579 cm⁻¹) species [66,67] indicates that ZrO₂ oxidizes NH₃ at low temperatures (150 °C).

Copper lead to an increase in NH₃ adsorption capacity, as evidenced by the differences in the spectra compared to those of ZrO₂ (Fig. 10b). In the presence of copper oxide species, both terminal hydroxyl groups associated with ZrO₂ decreased. NH₃ uptake was also greatly enhanced upon Cu addition, which can be explained by the relative ease by which Cu forms complexes with NH₃ [68]. All of the Lewis-bound NH₃ peaks increased relative to the bare support. Additional peaks were formed at 3151 and 1468 cm⁻¹, which can be assigned to NH₄⁺ species coordinated to Brønsted acid sites [62]. The broad signal spanning the region from 3400 to 2500 cm⁻¹ stems from the hydrogen-bonded NH₃ molecules [69]. Due to this rather broad background, the low-frequency bending region provides a more direct way of assessing the amount of NH₃ and NH₄⁺ species adsorbed. While the presence of copper oxide species imparted Brønsted functionality to the material, the Lewis acid sites remained the dominant adsorption centers for NH₃. Hence, the activity enhancement due to Cu loading can be attributed to the presence of redox-active Cu Lewis acid sites and not to the formed Brønsted acid sites, as observed on Cu-exchanged zeolites [70].

It is important to note that not all hydroxyl groups in Cu/ZrO₂ act as Brønsted acid sites because the strong negative hydroxyl bands at 3672 and 3763 cm⁻¹ did not change accordingly when passing from ZrO₂ to Cu/ZrO₂ and upon appearance of the NH₄⁺ peak at 1468 cm⁻¹. Hence, these -OH groups are most likely bonded with nitrite/nitrate species and possibly with weakly bonded or hydrogen-bonded NH₃. The nitrite peak at 1185 cm⁻¹ was visible also over Cu/ZrO₂, and two new bands appeared at 1288 and 1270 cm⁻¹, which can be assigned to either bidentate nitrate or nitrite species [66,71]. The direct oxidation of NH₃ at 150 °C is also reflected in the catalytic data shown in Fig. 5.

The C–H signal at 2875 cm⁻¹, which shifted to 2848 cm⁻¹ upon NH₃ introduction, reveals that even after calcination at 600 °C for 4 h and then at 700 °C for another 4 h, ZrO₂ still retained some organic precursors. While the presence of trace precursors is unwanted, calcination at higher temperature is discouraged to prevent the collapse of the mesoporous structure of the material. The presence of Cu afforded complete removal of these species at 600 °C, which is suggestive of the strong oxidative properties of copper oxide species [72,73].

3.4.2. Reaction of adsorbed NH₃ with NO

After NH₃ adsorption and cut-off (30 min) NO was introduced to convert the remaining NH₃ on the surface. Fig. 11 shows the *in situ* DRIFT spectra during NO adsorption over ZrO₂ and 3%Cu/ZrO₂ during the first 3 min and after 30 min. The lack of peaks at 1602 and 1185 cm⁻¹ in the spectrum recorded just before NO introduction (Fig. 11a) indicates that both NH₃ and nitrate species did not remain on ZrO₂ after 30 min. This could be explained by the weak adsorption of NH₃ and nitrate species to the Zr⁴⁺ centers or -OH groups, and by the oxidation of adsorbed NH₃ to NO-derived species. Upon addition of NO, the nitrite peak at 1185 cm⁻¹ increased, concomitant with the further decrease of the signals from the hydroxyl groups. In the absence of any residual NH₃ on the surface, no SCR reaction took place over ZrO₂ upon NO introduction.

On the contrary, a significant portion of NH₃ and NO-derived species remained on the surface of Cu/ZrO₂ even after prolonged purging (Fig. 11b), possibly indicating that both ligands coexist in one Cu²⁺ center and remain stable at low temperature [74]. Hence, the residual NH₃ reacted with NO to form the SCR products, including water, whose presence is provided by the increased absorption in the region of 3700–3500 cm⁻¹. The bending mode of physisorbed water at 1616 cm⁻¹ [75] is masked by the signal of nitrate species at 1586 and 1608 cm⁻¹, which formed together with nitrite species upon NO introduction. The appearance of a peak centered at 1506 cm⁻¹ may suggest the existence of nitrate species with different geometry on Cu/ZrO₂ [76], which was not observed on ZrO₂.

4. Conclusion

The one-step sol-gel synthesis procedure resulted in a mesoporous material with highly dispersed copper oxide. XRD did not show any copper oxide crystallites up to 6% loading, while CuO was apparent at 15% loading. While the specific dispersion of copper in these samples has not yet been determined, these results show the possibility of synthesizing well-dispersed catalysts with high metal loading.

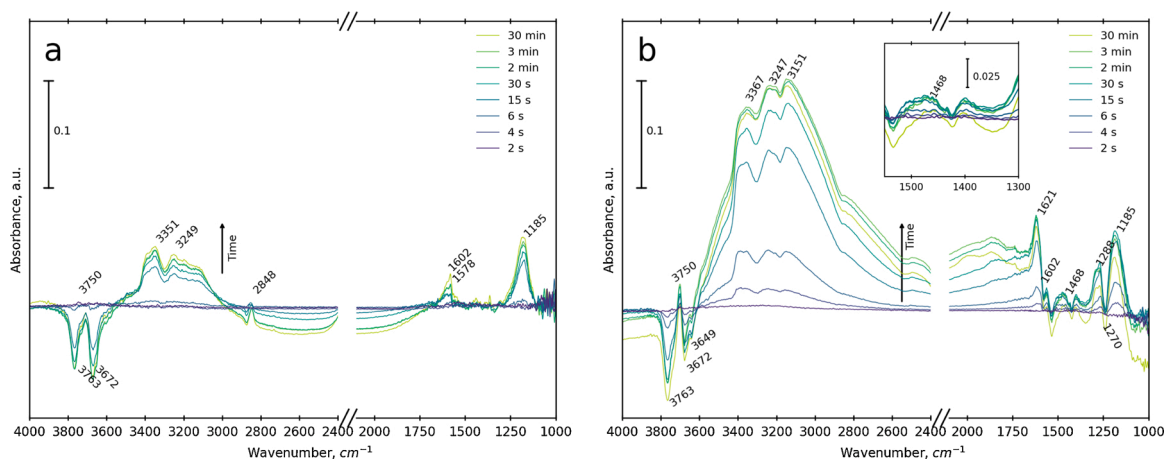A hydrothermal treatment was used to test the stability of the

Fig. 10. *In situ* DRIFTS during NH₃ adsorption over ZrO₂ (a), and over 3%Cu/ZrO₂ (b) at 150 °C. The inset in (b) shows the region 1550 cm⁻¹ to 1300 cm⁻¹ in detail. A flow of 5 vol% O₂ and 1000 ppm NH₃ in Ar was fed to the IR cell during the adsorption. The y-axes of (a) and (b) are equally scaled for better comparison of absorption of the two samples.
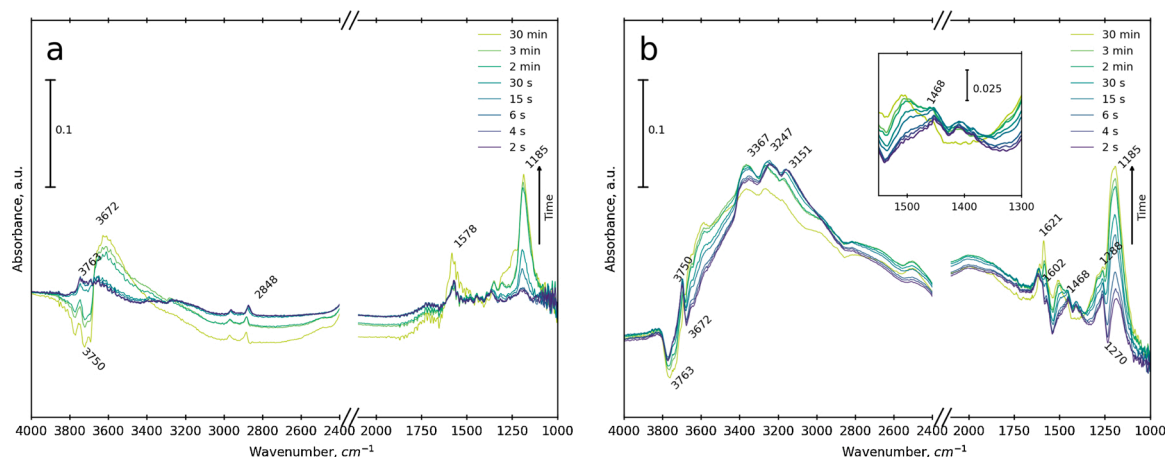
Fig. 11. *In situ* DRIFTS during reaction of adsorbed NH_3 with NO over ZrO_2 (a) and over 3%Cu/ZrO_2 (b) at 150 °C. A flow of 5 vol% O_2 and 1000 ppm NO in Ar was fed to the IR cell while spectra were collected. The y-axes of (a) and (b) are equally scaled for better comparison of absorption of the two samples.

materials. This caused some sintering of the zirconia support, leading to substantial loss of specific surface area and increase in pore size. The hydrothermally treated materials also appeared more crystalline in XRD. However, the treatment did not have a significant effect on the SCR performance of the samples, indicating that the copper sites were not severely affected by the treatment.

The Cu/ZrO_2 catalysts show promising SCR activity at low temperatures. At high temperatures there were issues with NH_3-loss to side reactions and formation of byproducts that impaired the NO_x conversion. Including steam in the feed stream lowered the overall SCR activity of the catalysts. As this effect is reversible, it is likely that this deactivation is caused by saturation of H_2O on the adsorption sites, blocking the reactants. 15%Cu/ZrO_2 was found to function well at low temperature, but showed poor conversion and selectivity above 350 °C. 6%Cu/ZrO_2 generally performed slightly better than 3%Cu/ZrO_2 under the applied conditions. Increasing the copper loading may therefore have a positive effect on the SCR performance, but this advantage has to be balanced against the risk of hydrothermal copper sintering, which was observed to a small degree for 6%Cu/ZrO_2.

The presence of redox-active Cu centers in the ZrO_2 structure increases NH_3 adsorption capacity by improving the Lewis functionality of the catalyst and increasing also the adsorption strength. Nitrate formation is observed when NO is adsorbed on the catalyst.

Steam and parasitic NH_3 oxidation are significant inhibiting factors for the catalysts, and poses problems that would need to be solved until these materials can be regarded as viable for commercial use. In principle, the concept of this synthesis is customizable and offers several opportunities to tune the properties of the catalyst to counteract these shortcomings. The possibility for optimization of this material is an interesting topic for further research.

Authors' Contribution

Conceptualization: O.H.B., M.R., S.K.R., R.J.G.N., D.F. Methodology: O.H.B., S.K.R., R.J.G.N., P.E.V., D.F. Formal analysis: O.H.B., S.K.R., R.J.G.N., P.E.V. Investigation: O.H.B., S.K.R., R.J.G.N., P.E.V. Writing – Original Draft: O.H.B., S.K.R., R.J.G.N. Writing – Review and editing: O.H.B., S.K.R., R.J.G.N., P.E.V., O.K., D.F., M.R. Visualization: O.H.B., S.K.R., P.E.V. Supervision: M.R., D.F., O.K. Project administration: M.R. Funding acquisition: M.R., D.F., O.K. All authors have read and agreed to the published version of the manuscript.

Declaration of Competing Interest

The authors report no declarations of interest.

Acknowledgements

References

[1] T.V. Johnson, A. Joshi, Review of deNOx technology for mobile applications, in: L. Lietti, L. Castoldi (Eds.), NOx Trap Catal. Technol. Fundam. Ind. Appl. 33, The Royal Society of Chemistry, 2018, pp. 1–35 (chapter 1).

[2] I. Nova, E. Tronconi, Urea-SCR Technology for deNOx After Treatment of Diesel Exhausts, Springer, New York, 2014.

[3] I. Bull, W.-M. Xue, P. Burk, R. Samuel Boorse, W.M. Jaglowski, G.S. Koermer, A. Moini, J.A. Patchett, J.C. Dettling, M.T. Caudle. US Patent US7,601,662B2: Copper CHA zeolite catalysts, 2009.

[4] J.H. Kwak, R.G. Tonkyn, D.H. Kim, J. Szanyi, C.H.F. Peden, J. Catal. 275 (2) (2010) 187–190.

[5] J.H. Kwak, D. Tran, S.D. Burton, J. Szanyi, J.H. Lee, C.H.F. Peden, J. Catal. 287 (3) (2012) 203–209.

[6] T.V. Johnson, Review of selective catalytic reduction (SCR) and related technologies for mobile applications, in: I. Nova, E. Tronconi (Eds.), Urea-SCR Technol. deNOx After Treat. Diesel Exhausts, Springer New York, New York, NY, 2014, pp. 3–31.

[7] A.M. Beale, F. Gao, I. Lezcano-Gonzalez, C.H.F. Peden, J. Szanyi, Chem. Soc. Rev. 44 (20) (2015) 7371–7405.

[8] E. Borfecchia, P. Beato, S. Svelle, U. Olsbye, C. Lamberti, S. Bordiga, Chem. Soc. Rev. 47 (22) (2018) 8097–8133.

[9] T.V.W. Janssens, H. Falsig, L.F. Lundegaard, P.N.R. Vennestrøm, S.B. Rasmussen, P. G. Moses, F. Giordanino, E. Borfecchia, K.A. Lomachenko, C. Lamberti, S. Bordiga, A. Godiksen, S. Mossin, P. Beato, ACS Catal. 5 (5) (2015) 2832–2845.

[10] K.A. Lomachenko, E. Borfecchia, C. Negri, G. Berlier, C. Lamberti, P. Beato, H. Falsig, S. Bordiga, J. Am. Chem. Soc. 138 (37) (2016) 12025–12028.

[11] A. Marberger, A.W. Petrov, P. Steiger, M. Elsener, O. Kröcher, M. Nachtegaal, D. Ferri, Nat. Catal. 1 (3) (2018).

[12] L. Han, S. Cai, M. Gao, J.Y. Hasegawa, P. Wang, J. Zhang, L. Shi, D. Zhang, Chem. Rev. 119 (19) (2019) 10916–10976.

[13] G. Centi, S. Perathoner, Appl. Catal. A: Gen. 132 (2) (1995) 179–259.

[14] Q. Yan, Y. Nie, R. Yang, Y. Cui, D. O'Hare, Q. Wang, Appl. Catal. A: Gen. 538 (2017) 37–50.

[15] Z. Si, D. Weng, X. Wu, J. Li, G. Li, J. Catal. 271 (1) (2010) 43–51.

[16] C.T. Kresge, M.E. Leonowicz, W.J. Roth, J.C. Vartuli, J.S. Beck, Nature 359 (6397) (1992) 710–712.

[17] C.J. Brinker, Y.F. Lu, A. Sellinger, H. Fan, Adv. Mater. 11 (7) (1999) 579–585.

[18] P. Krawiec, E. Kockrick, P. Simon, G. Auffermann, S. Kaskel, Chem. Mater. 18 (11) (2006) 2663–2669.

[19] Z.-X. Li, F.-B. Shi, L.-L. Li, T. Zhang, C.-H. Yan, Phys. Chem. Chem. Phys. 13 (7) (2011) 2488–2491.

[20] J. Fonseca, N. Bion, Y.E. Licea, C.M. Morais, M. Do Carmo Rangel, D. Duprez, F. Epron, Nanoscale 11 (3) (2019) 1273–1285.

[21] J. Liu, X. Shi, Y. Shan, Z. Yan, W. Shan, Y. Yu, Environ. Sci. Technol. 52 (20) (2018) 11769–11777.
[22] B. Zhao, R. Ran, X. Wu, D. Weng, X. Wu, C. Huang, Catal. Commun. 56 (2014) 36–40.
[23] I. Matsukuma, S. Kikuyama, R. Kikuchi, K. Sasaki, K. Eguchi, Appl. Catal. B: Environ. 37 (2) (2002) 107–115.
[24] K. Eguchi, M. Watabe, S. Ogata, H. Arai, J. Catal. 158 (2) (1996) 420–426.
[25] S.K. Das, M.K. Bhunia, A.K. Sinha, A. Bhaumik, J. Phys. Chem. C 113 (20) (2009) 8918–8923.
[26] S. Liu, H. Wang, Y. Wei, R. Zhang, S. Royer, ACS Appl. Mater. Interfaces 11 (25) (2019) 22240–22254.
[27] N. Apostolescu, B. Geiger, K. Hizbullah, M.T. Jan, S. Kureti, D. Reichert, F. Schott, W. Weisweiler, Appl. Catal. B: Environ. 62 (1–2) (2006) 104–114.
[28] D. Pietrogiacomi, D. Sannino, A. Magliano, P. Ciambelli, S. Tuti, V. Indovina, Appl. Catal. B: Environ. 36 (3) (2002) 217–230.
[29] Z. Si, D. Weng, X. Wu, Y. Jiang, B. Wang, Catal. Sci. Technol. 1 (3) (2011) 453–461.
[30] D. Pietrogiacomi, D. Sannino, S. Tuti, P. Ciambelli, V. Indovina, M. Occhiuzzi, F. Pepe, Appl. Catal. B: Environ. 21 (2) (1999) 141–150.
[31] S. Djerad, B. Geiger, F.J.P. Schott, S. Kureti, Catal. Commun. 10 (7) (2009) 1103–1106.
[32] K. Świrk, Y. Wang, C. Hu, L. Li, P. Da Costa, G. Delahay, Catalysts 11 (1) (2021) 55.
[33] Q. Yuan, A.-X. Yin, C. Luo, L.-D. Sun, Y.-W. Zhang, W.-T. Duan, H.-C. Liu, C.-H. Yan, J. Am. Chem. Soc. 130 (11) (2008) 3465–3472.
[34] G.S. Armatas, A.P. Katsoulidis, D.E. Petrakis, P.J. Pomonis, J. Mater. Chem. 20 (39) (2010) 8631–8638.
[35] S. Grant, A. Vinu, S. Pikus, M. Jaroniec, Colloids Surf. A: Physicochem. Eng. Aspects 385 (1–3) (2011) 121–125.
[36] G.J.B. Voss, E.A. Chavez Panduro, A. Midttveit, J.B. Fløystad, K. Høydalsvik, A. Gibaud, D.W. Breiby, M. Rønning, J. Mater. Chem. A 2 (25) (2014) 9727–9735.
[37] S. Brunauer, E. Emmett, E. Teller, J. Am. Chem. Soc. 60 (2) (1938) 309–319.
[38] E.P. Barrett, L.G. Joyner, P.P. Halenda, J. Am. Chem. Soc. 73 (1) (1951) 373–380.
[39] A. Vaitkus, A. Merkys, S. Gražulis, J. Appl. Crystallogr. 54 (2) (2021) 661–672.
[40] M. Quirós, S. Gražulis, S. Girdzijauskaitè, A. Merkys, A. Vaitkus, J. Cheminform. 10 (1) (2018) 1–17.
[41] A. Merkys, A. Vaitkus, J. Butkus, M. Okulič-Kazarinas, V. Kairys, S. Gražulis, J. Appl. Crystallogr. 49 (2016) 292–301.
[42] S. Gražulis, A. Merkys, A. Vaitkus, M. Okulič-Kazarinas, J. Appl. Crystallogr. 48 (1) (2015) 85–91.
[43] S. Gražulis, A. Daškevič, A. Merkys, D. Chateigner, L. Lutterotti, M. Quirós, N. R. Serebryanaya, P. Moeck, R.T. Downs, A. Le Bail, Nucleic Acids Res. 40 (D1) (2012) 420–427.
[44] S. Gražulis, D. Chateigner, R.T. Downs, A.F.T. Yokochi, M. Quirós, L. Lutterotti, E. Manakova, J. Butkus, P. Moeck, A. Le Bail, J. Appl. Crystallogr. 42 (4) (2009) 726–729.
[45] R.T. Downs, M. Hall-Wallace, Am. Mineral. 88 (2003) 247–250.
[46] G. Katz, J. Am. Ceram. Soc. 54 (10) (1971), pp. 531–531.
[47] J.D. McCullough, K.N. Trueblood, Acta Crystallogr. 12 (7) (1959) 507–511.
[48] G. Tunell, E. Posnjak, C.J. Ksanda, Zeitschrift für Krist. – Cryst. Mater. 90 (1–6) (1935).

[49] B. Zhang, S. Zhang, B. Liu, H. Shen, L. Li, RSC Adv. 8 (23) (2018) 12733–12741.
[50] R.J.G. Nuguid, D. Ferri, O. Kröcher, Emiss. Control Sci. Technol. 5 (4) (2019) 307–316.
[51] J.J.P. Biermann, F.J.J.G. Janssen, J.R.H. Ross, Appl. Catal. A: Gen. 86 (2) (1992) 165–179.
[52] G. Centi, S. Perathoner, D. Biglino, E. Giamello, Adsorption and Reactivity of NO on Copper-on-Alumina Catalysts: I. Formation of Nitrate Species and Their Influence on Reactivity in NO and NH$_3$ Conversion, 1995.
[53] M. Amblard, R. Burch, B.W.L. Southward, Catal. Lett. 68 (1–2) (2000) 105–108.
[54] S. Brandenberger, O. Kröcher, A. Tissler, R. Althoff, Catal. Rev. 50 (4) (2008) 492–531.
[55] T. Yu, T. Hao, D. Fan, J. Wang, M. Shen, W. Li, J. Phys. Chem. C 118 (13) (2014) 6565–6575.
[56] J. Li, H. Chang, L. Ma, J. Hao, R.T. Yang, Catal. Today 175 (1) (2011) 147–156.
[57] U.S. Ozkan, Y. Cai, M.W. Kumthekar, L.P. Zhang, Role of Ammonia Oxidation in Selective Catalytic Reduction of Nitric Oxide Over Vanadia Catalysts, 1993.
[58] H. Sjövall, L. Olsson, E. Fridell, R.J. Blint, Appl. Catal. B: Environ. 64 (3–4) (2006) 180–188.
[59] M. Iwasaki, Mechanistic aspect of NO-NH3-O2 reacting system, in: I. Nova, E. Tronconi (Eds.), Urea-SCR Technol. deNOx After Treat. Diesel Exhausts, Springer New York, 2014.
[60] P.O. Graf, D.J.M. de Vlieger, B.L. Mojet, L. Lefferts, J. Catal. 262 (2) (2009) 181–187.
[61] M. Kantcheva, Appl. Catal. B: Environ. 42 (1) (2003) 89–109.
[62] J.K. Lai, I.E. Wachs, ACS Catal. 8 (7) (2018) 6537–6551.
[63] A. Corma, V. Fornès, E. Ortega, J. Catal. 92 (2) (1985) 284–290.
[64] R.J.G. Nuguid, D. Ferri, A. Marberger, M. Nachtegaal, O. Kröcher, ACS Catal. 9 (8) (2019) 6814–6820.
[65] G. Ramis, G. Busca, V. Lorenzelli, P. Forzatti, Appl. Catal. 64 (C) (1990) 243–257.
[66] D. Yang, J. Li, M. Wen, C. Song, Catal. Today 139 (1–2) (2008) 2–7.
[67] H. He, J. Wang, Q. Feng, Y. Yu, K. Yoshida, Appl. Catal. B: Environ. 46 (2) (2003) 365–370.
[68] A.H. Clark, R.J.G. Nuguid, P. Steiger, A. Marberger, A.W. Petrov, D. Ferri, M. Nachtegaal, O. Kröcher, ChemCatChem 12 (5) (2020) 1429–1435.
[69] A. Zecchina, L. Marchese, S. Bordiga, C. Pazè, E. Gianotti, J. Phys. Chem. B 101 (48) (1997) 10128–10135.
[70] Y. Zhang, Y. Peng, K. Li, S. Liu, J. Chen, J. Li, F. Gao, C.H.F. Peden, ACS Catal. 9 (7) (2019) 6137–6145.
[71] Y. Chi, S.S.C. Chuang, J. Catal. 190 (1) (2000) 75–91.
[72] D. Terribile, A. Trovarelli, C. De Leitenburg, A. Primavera, G. Dolcetti, Catal. Today 47 (1–4) (1999) 133–140.
[73] M. Zimowska, A. Michalik-Zym, R. Janik, T. Machej, J. Gurgul, R.P. Socha, J. Podobiński, E.M. Serwicka, Catal. Today 119 (1–4) (2007) 321–326.
[74] C. Negri, E. Borfecchia, M. Cutini, K.A. Lomachenko, T.V.W. Janssens, G. Berlier, S. Bordiga, ChemCatChem 11 (16) (2019) 3828–3838.
[75] A. Marberger, D. Ferri, M. Elsener, O. Kröcher, Angew. Chem. Int. Ed. 55 (39) (2016) 11989–11994.
[76] B. Azambre, L. Zenboury, A. Koch, J.V. Weber, J. Phys. Chem. C 113 (30) (2009) 13287–13299.